Deviational simulation of phonon transport in graphene ribbons with ab initio scattering

Colin D. Landon and Nicolas G. Hadjiconstantinou

Articles you may be interested in

Size and boundary scattering controlled contribution of spectral phonons to the thermal conductivity in graphene ribbons
J. Appl. Phys. **115**, 063507 (2014); 10.1063/1.4865744

Monte Carlo simulation of phonon transport in silicon including a realistic dispersion relation
J. Appl. Phys. **114**, 154312 (2013); 10.1063/1.4826367

Lattice thermal conductivity of graphene nanoribbons: Anisotropy and edge roughness scattering
Appl. Phys. Lett. **98**, 141919 (2011); 10.1063/1.3569721

Monte Carlo study of phonon dynamics in III-V compounds
J. Appl. Phys. **109**, 063511 (2011); 10.1063/1.3553409

Contribution of d -band electrons to ballistic transport and scattering during electron-phonon nonequilibrium in nanoscale Au films using an ab initio density of states
J. Appl. Phys. **106**, 053512 (2009); 10.1063/1.3211310

Deviational simulation of phonon transport in graphene ribbons with *ab initio* scattering

Colin D. Landon and Nicolas G. Hadjiconstantinou
Department of Mechanical Engineering, Massachusetts Institute of Technology, Cambridge, Massachusetts 02139, USA

We present a deviational Monte Carlo method for solving the Boltzmann-Peierls equation with *ab initio* 3-phonon scattering, for temporally and spatially dependent thermal transport problems in arbitrary geometries. Phonon dispersion relations and transition rates for graphene are obtained from density functional theory calculations. The *ab initio* scattering operator is simulated by an energy-conserving stochastic algorithm embedded within a deviational, low-variance Monte Carlo formulation. The deviational formulation ensures that simulations are computationally feasible for arbitrarily small temperature differences, while the stochastic treatment of the scattering operator is both efficient and exhibits no timestep error. The proposed method, in which geometry and phonon-boundary scattering are explicitly treated, is extensively validated by comparison to analytical results, previous numerical solutions and experiments. It is subsequently used to generate solutions for heat transport in graphene ribbons of various geometries and evaluate the validity of some common approximations found in the literature. Our results show that modeling transport in long ribbons of finite width using the homogeneous Boltzmann equation and approximating phonon-boundary scattering using an additional homogeneous scattering rate introduces an error on the order of 10% at room temperature, with the maximum deviation reaching 30% in the middle of the transition regime. © *2014 AIP Publishing LLC.* [http://dx.doi.org/10.1063/1.4898090]

I. INTRODUCTION

Since Novoselov and Geim's landmark work on graphene in 2004,[1] a vast amount of theoretical and experimental research has attempted to characterize the thermal properties of this two-dimensional material. While the general consensus is that the thermal conductivity of suspended graphene is greater than 2000 W/m K at room temperature,[2–4] sometimes contradictory findings of various approaches (molecular dynamics,[5–8] Boltzmann-Peierls,[9–14] Landauer,[4,15] non-equilibrium Green's function,[16,17] optical thermometry experiments[2,3,7,18–20]) have led to considerable confusion regarding the fundamental physics of thermal transport in graphene. One example relevant to this work is the size dependence of thermal conductivity of unstrained graphene devices, which has been predicted to diverge with increasing device size,[21–24] but for which conclusive experimental evidence is lacking.[8,25]

An exhaustive review of the ongoing discussion of thermal transport in graphene is beyond the scope of this paper whose *primary* objective is the presentation and validation of a new method for solving the Boltzmann-Peierls equation (BPE) with *ab initio* scattering for temporally and spatially dependent problems. The proposed method is based on the deviational simulation Monte Carlo framework used to simulate both rarefied gases[26–28] and phonon transport in the relaxation-time approximation.[29–31] In the present paper, it is extended to include phonon dispersion relations and, via the linearized *ab initio* three phonon scattering operator,[32–34] anharmonic force constants calculated from density functional perturbation theory (DFPT).[35] Our hope is that this method, which we will refer to as linearized *ab initio*

phonon-low variance deviational simulation Monte Carlo (LAIP-LVDSMC), will provide insight into kinetic size effects in heat transport in two-dimensional materials, and that it will find use in modeling systems and devices at the mesoscale and microscale. Our formulation does not consider phonon confinement or coherence effects[36–39] and is therefore most appropriate for length scales larger than approximately 100 nm. At these lengthscales, significant kinetic (ballistic) effects still persist as shown, for example, by recent experimental measurements[8] of the effective thermal conductivity of graphene ribbons of width 1.5 μm and lengths ranging from hundreds of nanometers to almost 10 μm.

In this paper, LAIP-LVDSMC is extensively validated using experimental results, previous numerical solutions of the homogeneous BPE, as well as analytical results. Following validation, we use LAIP-LVDSMC to study some aspects of transport in graphene ribbons, paying particular attention to explicit treatment of the ribbon geometry and phonon-boundary interaction. Our results show that state of the art BPE solutions,[9,12,14] which rely on approximate treatments of boundary scattering, may under-predict the thermal conductivity of long ribbons of finite width by 10%–30% at room temperature.

II. BACKGROUND

The BPE

$$\frac{\partial n}{\partial t} + \boldsymbol{v}(\boldsymbol{q}, s) \cdot \nabla_{\boldsymbol{x}} n = \left[\frac{\partial n}{\partial t}\right]_{\text{scatt}}, \quad (1)$$

describes the dynamics of the phonon distribution function $n(\boldsymbol{x}, \boldsymbol{q}, s, t)$, where $\boldsymbol{v}$ is the phonon group velocity, $\boldsymbol{x}$ denotes

spatial position, q is the reciprocal space wavevector, s is the phonon polarization, and t is the time.

Due to the complexity associated with the *ab initio* representation of scattering processes, the scattering operator (modeled by the RHS of (1)) is frequently approximated using the phenomenological single mode relaxation time (SMRT) approximation, which models scattering events as relaxation processes towards the local equilibrium. Despite being rather crude, the SMRT approximation has been remarkably successful in describing thermal transport as mediated by phonons in three-dimensional materials.[40,41] However, in two-dimensional materials this model fails to reproduce the details of phonon-phonon scattering obtained using *ab initio* modeling.[9,10,12,13]

As a result, in this work, we consider the *ab initio* three-phonon scattering operator[34,42] (in two dimensions) given by

$$
\left[\frac{\partial n_\lambda}{\partial t}\right]_{\text{scatt}} = \frac{A_{\text{uc}}}{2\pi\hbar^2} \sum_{s',s''} \int d^2\boldsymbol{q}' |\tilde{\mathcal{V}}_3(-\lambda, -\lambda', \lambda'')|^2 \delta_{\text{I}}
$$
$$
\times \left((n_\lambda + 1)(n_{\lambda'} + 1)n_{\lambda''} - n_\lambda n_{\lambda'}(n_{\lambda''} + 1)\right)
$$
$$
+ \frac{A_{\text{uc}}}{4\pi\hbar^2} \sum_{s',s''} \int d^2\boldsymbol{q}' |\tilde{\mathcal{V}}_3(-\lambda, \lambda', \lambda'')|^2 \delta_{\text{II}}
$$
$$
\times \left((n_\lambda + 1)n_{\lambda'}n_{\lambda''} - n_\lambda(n_{\lambda'} + 1)(n_{\lambda''} + 1)\right), \quad (2)
$$

where, in the interest of simplicity, the spatial and time dependence of the distribution function are not shown explicitly and λ is used to denote the combined dependence of n on q and s. Here, A_{uc} is the material unit cell area, $\tilde{\mathcal{V}}_3(-\lambda, -\lambda', \lambda'')$ denotes the interaction strength of the corresponding three-phonon process,[34] while $\delta_{\text{I}} = \delta(-\omega_\lambda - \omega_{\lambda'} + \omega_{\lambda''})$ imposes energy conservation for type-I processes and $\delta_{\text{II}} = \delta(-\omega_\lambda + \omega_{\lambda'} + \omega_{\lambda''})$ for type-II processes; ω_λ denotes the frequency of phonon mode λ.

Solution of the BPE with the *ab initio* scattering operator has only recently been made feasible by using an iterative formulation[42–46] to yield the material response to a constant (and small) temperature gradient in the absence of boundaries. Even more recently, a variational formulation for solving the same class of problems has also been developed.[47] Both formulations assume spatially homogeneous, steady state, linearized conditions; finite-width graphene ribbons are approximately treated by modeling transverse boundaries via an additional (homogenous) scattering rate.[9,10,12,14]

The LAIP-LVDSMC method developed here can be used to obtain solutions of the BPE with *ab initio* scattering for more general problems exhibiting arbitrary spatial and temporal variations. It originates from the LVDSMC class of methods[30,31,48–52] for simulating the Boltzmann transport equation. LVDSMC methods achieve computational efficiency[26,27,53] by simulating only the deviation from a suitably chosen equilibrium distribution. For phonon systems, this is given by $n_\lambda^{\text{d}} = n_\lambda - n_\lambda^0$, where the equilibrium (control)[26] distribution is the Bose-Einstein distribution $n_\lambda^0 = n^{\text{BE}}(\omega_\lambda; T_0)$ parametrized by the equilibrium temperature T_0; the latter may be chosen to vary in space ($T_0 = T_0(\boldsymbol{x})$) as a means of improving variance reduction or simulating temperature gradients in the material.[30,31,48,49]

III. MATERIAL MODEL

The material model for this method is comprised of second and third order force constants, which for the present study was calculated using density functional theory (DFT) and perturbation theory.[35] Calculations were made using the local density approximation with the PZ parametrization,[54] and a lattice parameter of 2.43287 Å. The phonon dispersion relation is shown for high symmetry directions in Figure 1; agreement with experimental results[55,56] is excellent. The phonon frequencies at high symmetry points shown in Table I also agree well with other DFT calculated dispersion relations.[57,58]

IV. COMPUTATIONAL METHOD

Due to the small temperature gradients of interest here, we consider the case of small deviation from equilibrium ($n_\lambda^{\text{d}} \ll n_\lambda^0$) to obtain the linearized form of the scattering operator[9,33,34]

$$
\left[\frac{\partial n_\lambda^{\text{d}}}{\partial t}\right]_{\text{scatt}} = \frac{A_{\text{uc}}}{2\pi\hbar^2} \sum_{s',s''} \int d^2\boldsymbol{q}' |\tilde{\mathcal{V}}_3(-\lambda, -\lambda', \lambda'')|^2 \delta_{\text{I}}
$$
$$
\times \left(\left(n_{\lambda''}^0 - n_\lambda^0\right)n_{\lambda'}^{\text{d}} + \left(n_\lambda^0 + n_{\lambda'}^0 + 1\right)n_{\lambda''}^{\text{d}} + \left(n_{\lambda''}^0 - n_{\lambda'}^0\right)n_\lambda^{\text{d}}\right)
$$
$$
+ \frac{A_{\text{uc}}}{4\pi\hbar^2} \sum_{s',s''} \int d^2\boldsymbol{q}' |\tilde{\mathcal{V}}_3(-\lambda, \lambda', \lambda'')|^2 \delta_{\text{II}}
$$
$$
\times \left(\left(n_{\lambda''}^0 - n_\lambda^0\right)n_{\lambda'}^{\text{d}} + \left(n_{\lambda'}^0 - n_\lambda^0\right)n_{\lambda''}^{\text{d}} - \left(n_{\lambda''}^0 + n_{\lambda'}^0 + 1\right)n_\lambda^{\text{d}}\right).
$$
$$
(3)
$$

We note that the assumption of small deviation from equilibrium is not required for the LVDSMC methodology, which is valid for arbitrary deviations from equilibrium.[59] Simulations of the non-linear operator (2) will, however, require a different treatment from the one described here.

A. Reciprocal space discretization

In order to facilitate efficient integration of (3) over $\boldsymbol{q}'$, we discretize the reciprocal space unit cell,[43,46,47,60] as shown in Figure 2, and use a two dimensional implementation of the linear tetrahedra method.[61,62] As a result, the linearized scattering operator can be written in the form[47,60]
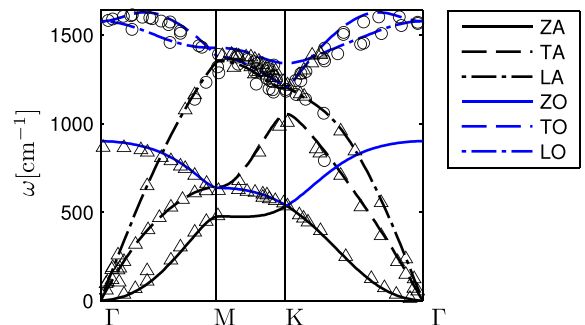

FIG. 1. Comparison of the phonon dispersion relation used in this work with neutron scattering experiments (circles[55] and triangles[56]).

TABLE I. Graphene dispersion relation at high symmetry points in units of cm^{-1}. This work uses a lattice parameter of 2.43287 Å and the LDA-PZ parameterization.[54]

Point	ZA	TA	LA	ZO	TO	LO
Γ	0	0	0	900.5	1577.4	1577.4
M	475.7	642.0	1352.9	636.7	1426.9	1377.1
K = K'	535.5	1053.7	1205.6	535.6	1340.9	1206.2

$$\left[\frac{\partial n_i^{\mathrm{d}}}{\partial t}\right]_{\mathrm{scatt}} = \sum_{j=1}^{N_{\mathrm{states}}} A_{ij} n_j^{\mathrm{d}}, \qquad (4)$$

where N_{states} is the number of discrete reciprocal states and i indexes the discrete state with wavevector $\boldsymbol{q}_i$ and polarization s_i. The transition matrix is given[60] by

$$A_{lm} = \frac{A_{\mathrm{uc}}}{2\pi\hbar^2} \frac{1}{n_m^0(n_m^0+1)}$$
$$\times \sum_{ijk} \left[N_{\mathrm{I}}(i,j,k) W_{\mathrm{I}}(i,j,k)\left(-\delta_{im}\delta_{ml} - \delta_{il}\delta_{jm} + \delta_{il}\delta_{km}\right) \right.$$
$$\left. + N_{\mathrm{II}}(i,j,k) W_{\mathrm{II}}(i,j,k)\left(-\delta_{im}\delta_{ml} + \delta_{il}\delta_{jm} + \delta_{il}\delta_{km}\right) \right], \quad (5)$$

where $W_{\mathrm{I}}(i,j,k)$ and $W_{\mathrm{II}}(i,j,k)$ are the coefficients arising from the linear interpolation,[60] $N_{\mathrm{I}}(i,j,k) = n_i^0 n_j^0 (n_k^0+1)$ and $N_{\mathrm{II}}(i,j,k) = \frac{1}{2}(n_i^0+1) n_j^0 n_k^0$.

For convenience in selecting momentum conserving processes, the discretization is chosen to include the Γ point. However, the three acoustic branch phonons at the Γ point are excluded because they do not satisfy the fundamental condition for existence,[63] namely, $\omega_\lambda \tau_\lambda > 1$, where τ_λ is the phonon mode lifetime. Because of this exclusion, the number of states is given by $N_{\mathrm{states}} = N_{\mathrm{side}}^2 - 3$, where N_{side} is the number of segments into which each reciprocal space basis vector is discretized.

In order to ensure strict energy conservation,[48] we simulate the energy distribution

$$f_i = \frac{2}{A_{\mathrm{uc}} N_{\mathrm{tri}} \delta} \hbar \omega_i n_i, \qquad (6)$$

where N_{tri} is the number of triangles in the reciprocal space discretization, and we use $\delta = 3.35$ Å as the nominal
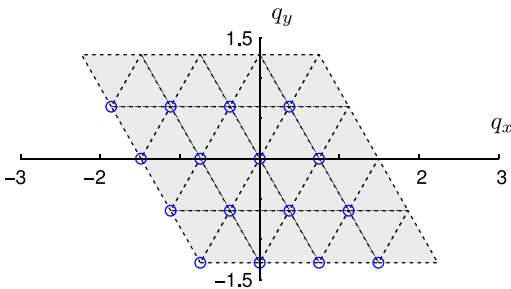

FIG. 2. Parallelepiped unit cell used to discretize reciprocal space (units are 10^{10} m^{-1}). Only the circled vertices are included in the computational mesh—vertices on the right and top boundaries are equivalent to those on the left and bottom boundaries, respectively, via periodicity. Here (for clarity), a $N_{\mathrm{states}} = 93$ discretization is shown—six branches with 16 states in each branch, the Γ point for the three acoustic branches being removed.

thickness of graphene.[64,65] Under this formulation, the BPE in the discretized reciprocal space becomes

$$\frac{\partial f_i^{\mathrm{d}}}{\partial t} + \boldsymbol{v}_i \cdot \nabla_{\boldsymbol{x}} f_i^{\mathrm{d}} + \boldsymbol{v}_i \cdot \nabla_{\boldsymbol{x}} f_i^0 = \sum_j B_{ij} f_j^{\mathrm{d}}, \qquad (7)$$

where $f_i^0 = (2/A_{\mathrm{uc}} N_{\mathrm{tri}} \delta)\hbar\omega_i n_i^0$ and $B_{ij} = (\omega_i/\omega_j)A_{ij}$.

We have found that due to numerical errors in the calculations of the third order force constants and due to finite discretization of the reciprocal space and the linear interpolation, the calculated transition matrix $B_{ij} = (\omega_i/\omega_j)A_{ij}$ does not conserve energy and momentum exactly. This creates numerical problems for our strictly (energy) conserving scattering scheme described in Sec. IV B 2. In this work, we used two numerical techniques to ameliorate this problem. First, the interaction term was symmetrized

$$6|\tilde{\mathcal{V}}_{3,\mathrm{sym}}(\lambda,\lambda',\lambda'')|^2 = |\tilde{\mathcal{V}}_3(\lambda,\lambda',\lambda'')|^2 + |\tilde{\mathcal{V}}_3(\lambda',\lambda,\lambda'')|^2$$
$$+ |\tilde{\mathcal{V}}_3(\lambda'',\lambda',\lambda)|^2 + |\tilde{\mathcal{V}}_3(\lambda'',\lambda,\lambda')|^2$$
$$+ |\tilde{\mathcal{V}}_3(\lambda',\lambda'',\lambda)|^2 + |\tilde{\mathcal{V}}_3(\lambda,\lambda'',\lambda')|^2 \quad (8)$$

to ensure required symmetries were satisfied. Second, a Lagrange multiplier optimization scheme[60] was used to construct an additive correction to $\boldsymbol{B}$, so that the latter satisfies energy conservation

$$\sum_i \left[\frac{\partial f_i^{\mathrm{d}}}{\partial t}\right]_{\mathrm{scatt}} = 0 = \sum_{ij} B_{ij} f_j^{\mathrm{d}} = \sum_j \underbrace{\left(\sum_i B_{ij}\right)}_{=0} f_j^{\mathrm{d}} \qquad (9)$$

and momentum conservation

$$\sum_i \mathbf{q}_i \left[\frac{\partial n_i^{\mathrm{d}}}{\partial t}\right]_{\mathrm{scatt}} = 0 = \sum_{ij} \frac{\mathbf{q}_i}{\omega_i} B_{ij}^{\mathrm{N}} f_j^{\mathrm{d}} = \sum_j \underbrace{\left(\sum_i \frac{\mathbf{q}_i}{\omega_i} B_{ij}^{\mathrm{N}}\right)}_{=0} f_j^{\mathrm{d}}$$
$$(10)$$

where $\boldsymbol{B}^{\mathrm{N}}$ denotes the part of the $\boldsymbol{B}$ matrix that contains only the normal scattering processes.

B. Low-variance Monte Carlo simulation

In the LVDSMC class of methods,[30,31,60] the distribution function is approximated using N_{parts} computational particles. This approximation can be expressed mathematically by writing

$$f_i^{\mathrm{d}} \approx \sum_{j=1}^{N_{\mathrm{parts}}} E_{\mathrm{eff}} \sigma_j \delta_{\lambda_j, \lambda_i} \delta(\boldsymbol{x} - \boldsymbol{x}_j), \qquad (11)$$

where E_{eff} is the effective energy that each computational particle represents and σ_j is the sign (± 1) of particle j. Equation (11) highlights the fact that this work uses a discrete representation of the reciprocal space required by the scattering model, but a continuous representation of physical space. In general, advantages of particle based approaches include efficient scaling in higher dimensions; importance

sampling;[27] natural, efficient, and accurate treatment of discontinuities in the distribution function;[26,27,66] and simple, intuitive algorithms.[67]

Integration of (7) in the LVDSMC formulation proceeds via a splitting algorithm,[68,69] which evolves the particle dynamics using decoupled advection and scattering steps in sequence, each of duration Δt. As described below, this formulation requires four main algorithmic ingredients, namely, initialization, sampling, scattering, and advection. Particular emphasis is given here to the scattering step, which is entirely new. The other ingredients have been discussed previously for three-dimensional materials (and continuous reciprocal space descriptions);[30,48] here, we focus on differences arising from the two-dimensional nature of the material and the discrete reciprocal space description.

1. Initialization

Initialization requires sampling particles from the appropriate distribution function representing the initial condition. In the general case of an arbitrary (non-equilibrium) initial distribution, $f_i(\boldsymbol{x}, t = 0)$, the deviational simulation needs to be initialized from the deviational distribution

$$f_i^{\mathrm{d}}(\boldsymbol{x}, t = 0) = f_i(\boldsymbol{x}, t = 0) - f_i^0. \tag{12}$$

This is achieved by generating particles from the distribution

$$|f_i(\boldsymbol{x}, t = 0) - f_i^0| \tag{13}$$

with sign $\mathrm{sgn}(f_i^{\mathrm{d}}(\boldsymbol{x}, t = 0))$. The number of such particles is determined from $N_{\mathrm{parts}}^{\mathrm{init}} = \sum_i |f_i^{\mathrm{d}}(\boldsymbol{x}, t = 0)|/E_{\mathrm{eff}}$. These particles can be generated by the method of acceptance-rejection.[60,67] More sophisticated methods for sampling distribution functions for LVDSMC simulations have been developed for the rarefied gas case[70] and may prove useful for phonon simulation.

For steady problems, it is most convenient to initialize the simulation from the reference (control) equilibrium so that $f_i^{\mathrm{d}}(\mathbf{x}, t = 0) = 0$. In that case, no particles need to be generated for initialization and the initial condition is represented exactly.

2. Scattering

The scattering step updates the particle distribution due to the action of the scattering operator over a timestep. In this case, the distribution after a timestep is known in terms of the generator

$$\boldsymbol{P}(\Delta t) = e^{\boldsymbol{B}\Delta t} = \sum_{k=0}^{\infty} \frac{\Delta t^k}{k!} \boldsymbol{B}^k,$$

namely,

$$f_i^{\mathrm{d}}(t + \Delta t) = \sum_j P_{ij}(\Delta t) f_j^{\mathrm{d}}(t). \tag{14}$$

Although at first glance this appears to resemble a Markov chain formulation, two significant differences make the former not applicable: first, the distribution f_i^{d} can take positive or negative values; second, the elements of the generator, P_{ij},

can be negative or greater than unity (a consequence of having negative off-diagonal elements in $\boldsymbol{B}$ due to three phonon coupling).

To account for the above complexity, we rewrite (14) in the form

$$f_i^{\mathrm{d}}(t + \Delta t) = \sum_j \frac{P_{ij}(\Delta t)}{\mathcal{P}_j} \left(\sum_{n=0}^{\infty} \left(2\frac{\mathcal{P}_j^-}{\mathcal{P}_j} \right)^n \right) f_j^{\mathrm{d}}(t), \tag{15}$$

where $\mathcal{P}_j^-$ is the sum of the absolute values of the negative elements in column j of $\boldsymbol{P}$, and $\mathcal{P}_j = \sum_{k=1}^{N_{\mathrm{states}}} |P_{kj}|$. Equation (15) can be implemented by repeating the following process for all particles: for a particle in state j with sign σ,

1. Transition particle to the state p given by

$$\sum_{i=1}^{p-1} |P_{ij}| \leq \mathcal{R}\mathcal{P}_j < \sum_{i=1}^{p} |P_{ij}|,$$

   where $\mathcal{R}$ is a uniform random variate in $[0, 1)$.
2. Assign a new sign to the particle: $\sigma' = \mathrm{sgn}(P_{pj}\sigma)$.
3. If $\sigma' \neq \sigma$, generate 2 more particles in state j, with sign σ and process each by going to step 1.

Here, we note that the scattering algorithm just described, by construction, exactly conserves energy. Also, since (14) is exact, this scheme introduces no timestep error; this is numerically demonstrated in Sec. V B. However, the complete simulation algorithm is first-order accurate in time due to the timestep error introduced by the splitting scheme. Higher-order accuracy can be achieved by symmetrizing the splitting scheme[30,70] and will be pursued in future work.

Moreover, assuming that the number of particles is proportional to N_{states} as suggested by numerical experiments,[60] the cost of the scattering step is expected to be of $O(N_{\mathrm{states}} \log(N_{\mathrm{states}}))$ operations, since the state to which each particle scatters can be found using a binary search method. This scaling is superior to a deterministic approach, in which the same step would take $O((N_{\mathrm{states}})^2)$ operations.

The generation of additional particles is, in general, undesirable and if measures are not taken, it can cause the simulation to become unstable. Stability is achieved by canceling positive and negative particles in the same reciprocal space state and the same spatial cell.[48] When cancellation takes place between particles at finite distance, discretization error is introduced, requiring that spatial cells be small (typically smaller than the mean free path). This is, in fact, the only form of spatial discretization error introduced by this algorithm.

3. Advection

The advection step simulates the left hand side of (7), and is typically implemented as two separate parts. The first part is the traditional advection step

$$\frac{\partial f_i^{\mathrm{d}}}{\partial t} + \boldsymbol{v}_i \cdot \nabla_{\boldsymbol{x}} f_i^{\mathrm{d}} = 0, \tag{16}$$

which describes ballistic motion of particles and is implemented by advecting each particle for the timestep duration,

namely, $\boldsymbol{x}_j(t + \Delta t) = \boldsymbol{x}_j(t) + \boldsymbol{v}_j(t)\Delta t$ for $j = 1, ..., N_{\text{parts}}$. If interrupted by an encounter with a boundary, the particle motion continues for the remaining part of the timestep after processing the associated boundary condition. The particle formulation lends itself naturally to the treatment of boundary conditions associated with phonon transport. Below, we describe boundaries at a prescribed temperature as an example.

The second part of the advection step implements the term

$$\boldsymbol{v}_i \cdot \frac{\partial f^{\text{BE}}(\omega_i; T)}{\partial T} \nabla_{\boldsymbol{x}} T_0(\boldsymbol{x}), \tag{17}$$

which is nonzero if the control temperature is chosen to be a function of space. As discussed in a number of previous publications for three dimensional[30,31,48] and for two-dimensional[60] materials, this can be implemented by treating (17) as a distribution from which

$$\frac{\left| \boldsymbol{v}_i \cdot \dfrac{\partial f^{\text{BE}}(\omega_i; T)}{\partial T} \nabla_{\boldsymbol{x}} T_0(\boldsymbol{x}) \right| \Delta t}{E_{\text{eff}}} \tag{18}$$

particles are generated per timestep. A variable control temperature can be useful for improving computational efficiency via improved variance reduction, or introducing a temperature gradient without explicitly simulating the physical dimension, in which the gradient exists.[30,48]

a. Boundaries at prescribed temperature. Consider a boundary at a fixed (prescribed) temperature T_{b} with inward normal (pointing into the material) $\hat{\mathbf{n}}_{\text{b}}$. The net heat flux across this boundary is given by

$$J_{E,\text{b}} = \sum_i \boldsymbol{v}_i \cdot \hat{\mathbf{n}}_{\text{b}} f_i^{\text{d}}. \tag{19}$$

Particles entering the domain from the boundary ($\boldsymbol{v}_i \cdot \hat{\mathbf{n}}_{\text{b}} > 0$) come from a known distribution, $f_i^{\text{b}} = f^{\text{BE}}(\omega_i; T_{\text{b}})$ $= (2/A_{\text{uc}} N_{\text{tri}} \delta) \hbar \omega_i n^{\text{BE}}(\omega_i; T_{\text{b}})$. Accordingly, the heat flux can be divided into incoming and outgoing components

$$J_{E,\text{b}} = \sum_{\{i | \boldsymbol{v}_i \cdot \hat{\mathbf{n}}_{\text{b}} > 0\}} \boldsymbol{v}_i \cdot \hat{\mathbf{n}}_{\text{b}} (f_i^{\text{b}} - f_i^0)$$
$$- \sum_{\{i | \boldsymbol{v}_i \cdot \hat{\mathbf{n}}_{\text{b}} < 0\}} |\boldsymbol{v}_i \cdot \hat{\mathbf{n}}_{\text{b}}| f_i^{\text{d}}. \tag{20}$$

Such a boundary condition can be implemented in the following manner: particles within the simulation that encounter the boundary during the advection step (described by the term $|\boldsymbol{v}_i \cdot \hat{\mathbf{n}}_{\text{b}}| f_i^{\text{d}}$) are discarded; particles representing the influx from the boundary

$$\sum_{\{i | \boldsymbol{v}_i \cdot \hat{\mathbf{n}}_{\text{b}} > 0\}} \boldsymbol{v}_i \cdot \hat{\mathbf{n}}_{\text{b}} (f^{\text{b}} - f_i^0) \tag{21}$$

are generated following the general procedure outlined in Sec. IV B 1, and described in more detail in previous works.[30,31,48,60]

Two special cases of this boundary condition are important for our simulation. The first is when the boundary

temperature is chosen to be the reference equilibrium temperature T_0. In this case, the particles encountering the boundary are removed and no additional particles need to be generated. The second is an adiabatic (diffuse) boundary. In this case, the particles encountering the boundary are used to determine the temperature of the boundary, T_{b}, by numerically inverting

$$\sum_{\{i | \boldsymbol{v}_i \cdot \hat{\mathbf{n}}_{\text{b}} > 0\}} \boldsymbol{v}_i \cdot \hat{\mathbf{n}}_{\text{b}} (f^{\text{BE}}(\omega_i; T_{\text{b}}) - f_i^0) = \sum_{\{i | \boldsymbol{v}_i \cdot \hat{\mathbf{n}}_{\text{b}} < 0\}} |\boldsymbol{v}_i \cdot \hat{\mathbf{n}}_{\text{b}}| f_i^{\text{d}}. \tag{22}$$

4. Sampling

Transport properties are sampled by dividing the physical domain into cells of volume $V_{\text{cell}} = A_{\text{cell}} \delta$. For example, the energy density in a cell of volume V_{cell} is

$$u_m = \frac{\sum_{\{j | \boldsymbol{x}_j \in \text{cell } m\}} E_{\text{eff}} \sigma_j}{V_{\text{cell}}} + u_{\text{eq}}(T_0), \tag{23}$$

where $u_{\text{eq}}(T_0)$ is the energy density at the reference temperature T_0 calculated from the equilibrium energy-temperature relation

$$u_{\text{eq}}(T_0) = \sum_i f^{\text{BE}}(\omega_i; T_0). \tag{24}$$

The heat flux in cell m is given by

$$\boldsymbol{J}_{E,m} = \frac{1}{V_{\text{cell}}} \sum_{\{j | \boldsymbol{x}_j \in \text{cell } m\}} E_{\text{eff}} \sigma_j \boldsymbol{v}_j. \tag{25}$$

These estimators have been variance-reduced[26,27] by separating out the equilibrium contribution to the estimator and evaluating it analytically. This strategy can significantly reduce stochastic noise and improve computational efficiency, particularly in problems where temperature differences are small.[30]

V. VALIDATION

In this section, we discuss some of the tests used to validate the method described in Sec. IV. More extensive validation tests can be found elsewhere.[60]

A. Thermal conductivity of infinitely large graphene sheets

The thermal conductivity of an infinity large graphene sheet can be calculated by solution of

$$\boldsymbol{v}_i \cdot \nabla_{\boldsymbol{x}} f_i^0 = \sum_j B_{ij} f_j^{\text{d}}, \tag{26}$$

which models a homogeneous material under the action of a temperature gradient. In previous work,[9,12,14] a related equation was solved using deterministic approaches. We repeated this (deterministic) calculation in order to validate our material model and the associated matrix $\boldsymbol{B}$: specifically, we

TABLE II. Convergence of the iterative solution thermal conductivity with respect to discretization N_{side}.

N_{side}	$\kappa_{xx,SMRT}$	$\kappa_{yy,SMRT}$	κ_{xx}	κ_{yy}
5	586.18	579.74	1474.41	1434.02
11	468.97	481.62	2584.32	2533.65
21	510.51	530.40	3099.31	3013.94
31	515.51	535.35	3272.60	3160.60
41	513.87	533.38	3345.17	3237.89
51	515.01	534.18	3467.55	3336.47
61	514.84	533.81	3539.02	3397.62
71	514.42	533.30	3554.41	3401.23
81	513.13	531.91	3591.68	3444.19

solved Eq. (26) using the deterministic iterative method of Omini and Sparavigna.[9,12,43]

Our results are shown in Table II. As the discretization is refined, the thermal conductivity converges towards a value of approximately 3500 W/m K, with no boundary or isotope scattering. We exclude the latter for clarity, and because it is reported to have a small effect in graphene.[14]

Table II also shows results obtained from the SMRT approximation defined by

$$B_{ij}^{SMRT} = B_{ij}\delta_{ij}. \qquad (27)$$

This approximation severely under predicts the thermal conductivity when calculated from actual scattering rates (i.e., using Eq. (27), as opposed to treating the relaxation times as adjustable parameters—see also Refs. 9 and 13).

Table III shows iterative solution results in the presence of additional homogeneous scattering[33,43,46,71] of the form

$$B_{ii}^{circ} = B_{ii} + \frac{v_i}{L_b} \qquad (28)$$

modeling[2,72,73] a Corbino membrane of diameter L_b; here, $v_i = ||\boldsymbol{v}_i||$. The results are in reasonable agreement with previous *ab initio* thermal transport simulations using empirical potentials and DFT/DFPT based force constants. We note that steps we took to enforce symmetry upon our transition rate matrix (see Eq. (8)) may account for the slightly lower thermal conductivities obtained with this method.

Figure 3 shows a comparison of our membrane results for a Corbino membrane with experimental measurements at various temperatures. Despite the large uncertainty in the experimental data due to uncertainties in the experimental

TABLE III. Thermal conductivity (along the Γ to M line where available) from this work and other sources as well as the relative importance of each branch in terms of total energy carried.

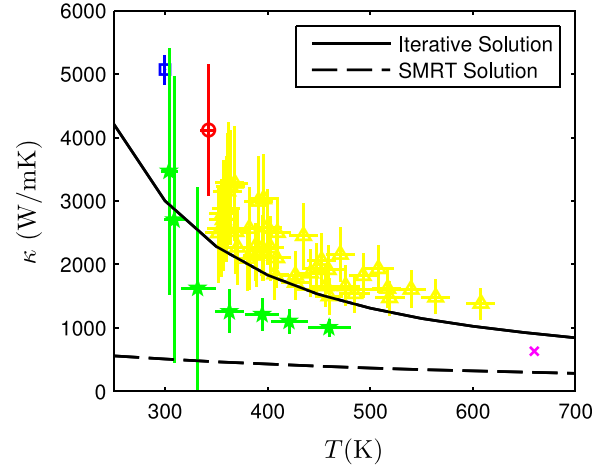| Source	κ	ZA (%)	TA (%)	LA (%)	ZO (%)
$N_{side} = 81, L_b = \infty$	3592	86.10	9.12	2.48	2.37
$N_{side} = 81, L_b = 10\mu m$	2984.1	82.96	10.83	3.60	2.65
Empirical potential[12]	3216	89	8	3	0
Empirical potential[9]	3435	76	15	9	0
DFT/DFPT[14]	3288–3596	76	15	8	0

FIG. 3. Temperature dependence of the iterative solution thermal conductivity compared to various recent experimental measurements (red circle,[19] blue square,[18] yellow triangles,[2] green stars,[3] and magenta cross[73]). Calculations used the symmetrized interaction term (8) and the Corbino membrane scattering rate (28) with $L_b = 10\mu m$.

procedure,[2] our results fit well within the trend of the data, similarly to previous *ab initio* BPE solutions.[9,12]

B. Homogeneous time-dependent problems

Is this section, we validate our simulation methodology, and the scattering operator treatment of Sec. IV B 2, in particular, by comparing the LAIP-LVDSMC solution of a homogeneous problem described by

$$\frac{\partial f_i^d}{\partial t} + \boldsymbol{v}_i \cdot \nabla_{\boldsymbol{x}} f_i^0 = \sum_j B_{ij} f_j^d, \qquad (29)$$

to a solution obtained using a simple Euler integration (deterministic) method. As in Eq. (26), the term $\boldsymbol{v}_i \cdot \nabla_{\boldsymbol{x}} f_i^0$ is a known "source term" representing an (externally) imposed temperature gradient, making this problem the time-dependent extension of the problem studied in Sec. V A. Figure 4 shows the resulting heat flux in the direction of the applied temperature gradient for the initial condition $f_i^d(t = 0) = 0$; the agreement between the two solutions is excellent. We also note that, although not shown in the figure, both transient solutions asymptotically $(t \to \infty)$
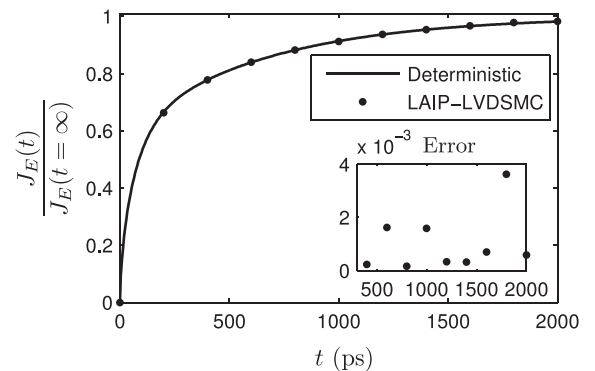

FIG. 4. Comparison of LAIP-LVDSMC simulation with a deterministic scheme for a time-dependent homogeneous problem.

match the solution of (26) obtained in Sec. V A. The latter is used to normalize the results and is denoted in the figure by $J_E(t = \infty)$.

C. Comparison with analytical solution of an SMRT model

Additional validation is provided using the closed form solution of the BPE for infinitely long ribbons with the SMRT scattering operator defined in (27).[50,74] Specifically, for an infinitely long ribbon of finite width we expect $f_i^{\rm d}$ to be a function of only the ξ coordinate (see Figure 5). At steady state and under the SMRT approximation, Eq. (7) then reduces to

$$v_i \sin(\theta_i)\frac{df_i^{\rm d}}{d\xi} + v_i \cos(\theta_i)\frac{dT}{d\eta}\frac{\partial f^{\rm BE}(\omega_i;T)}{\partial T}\Big|_{T_0} = B_{ii}f_i^{\rm d}, \quad (30)$$

where θ_i is the angle between the wavevector and the η axis, as shown in Figure 5, and $dT/d\eta$ is the imposed temperature gradient. The solution of this equation subject to diffuse boundary conditions is

$$f_i^{\rm d}(\xi) = \begin{cases} f_i^{\rm d,\infty}\left(1 - \exp\left(-\dfrac{\xi}{Kn_i \sin(\theta_i)}\right)\right) & 0 \le \theta_i < \pi \\[2ex] f_i^{\rm d,\infty}\left(1 - \exp\left(-\dfrac{\xi - 1}{Kn_i \sin(\theta_i)}\right)\right) & \pi \le \theta_i < 2\pi \end{cases}$$
$$(31)$$

where the mode specific Knudsen number is given by

$$Kn_i = \frac{v_i}{B_{ii}W}. \quad (32)$$

Here,

$$f_i^{\rm d,\infty} = -B_{ii}^{-1}v_i \cos(\theta_i)\frac{dT}{d\eta}\frac{\partial f^{\rm BE}(\omega_i;T)}{\partial T}\Big|_{T_0}. \quad (33)$$

Consequently, the exact solution for the width-averaged heat flux ($\bar{\boldsymbol{J}}_E^{\rm SMRT} = 1/W \int_0^1 \boldsymbol{J}_E^{\rm SMRT} d\xi$) for a ribbon of volume $LW\delta$ is[60]

$$\bar{\boldsymbol{J}}_E^{\rm SMRT} = \sum_{i=1}^{N_{\rm states}} \boldsymbol{v}_i f_i^{\rm d,\infty}$$
$$\times \left(1 - Kn_i|\sin(\theta_i)|\left(1 - \exp\left(-\frac{1}{Kn_i|\sin(\theta_i)|}\right)\right)\right). \quad (34)$$

This expression must still be evaluated using the reciprocal space discretization; in order to make the comparison with simulation as precise as possible, we use the same reciprocal space discretization as in the particle simulation, namely, $N_{\rm states} = 5397$.

Figure 6 shows a comparison between the prediction of Eq. (34) for the axial heat flux $\bar{J}_{E,\eta}^{\rm SMRT}$ and spatially dependent (SMRT) LVDSMC results for the same problem. Note that the simulation only considers the transverse ribbon direction by utilizing an axially variable control temperature (see Eq. (17)) to impose the axial temperature gradient. As expected, the analytical solution and the simulation are in essentially perfect agreement (less than 1% discrepancy). A comparison of profiles of the axial component of the heat flux for various ribbon widths is also shown in Figure 7. The small error present is due to the statistical uncertainty associated with the Monte Carlo and the finite spatial discretization of the Monte Carlo simulation.

D. Additional validation

Additional validation can be found in Sec. VI B, where it is demonstrated that LAIP-LVDSMC simulations recover the analytically known[75,76] ballistic limit for infinitely wide but short ribbons subject to an axial temperature gradient.

VI. SIMULATION OF HEAT TRANSPORT IN GRAPHENE RIBBONS

We now discuss computational results for heat transport along graphene ribbons with diffusely reflecting transverse boundaries (see Figure 5) at room temperature (300 K). These results are obtained using the LAIP-LVDSMC methodology developed in this paper, and described in Sec. IV which uses the linearized *ab initio* scattering operator (3). In other words, transport is explicitly resolved in the ribbon geometry and boundaries are explicitly treated rather than being approximated by additional homogeneous scattering. Specifically, the longitudinal boundaries are modeled as prescribed temperature boundaries, while the transverse boundaries are modeled as diffuse adiabatic (see Figure 5).

FIG. 6. Comparison between the analytical solution for the axial heat flux in long graphene ribbon with diffusely reflecting boundaries under the SMRT approximation (34) and (SMRT) LAIP-LVDSMC results. Both results are normalized by the axial heat flux for a homogeneous material ($J_{E,\rm homo,\eta}^{\rm SMRT}$) under the same temperature gradient. The error is defined as the absolute value of the difference between the two results.
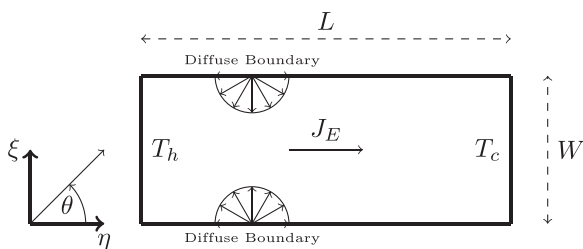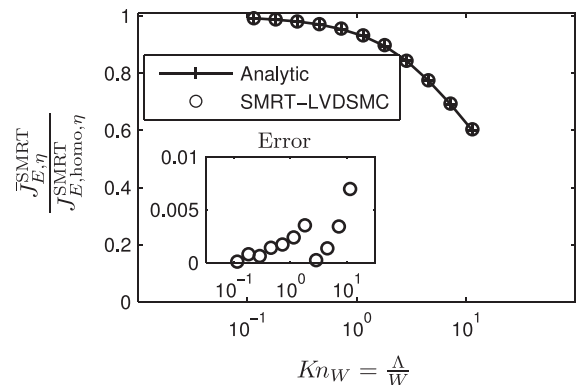

FIG. 5. Schematic of graphene ribbon with diffuse boundaries. Coordinates η and ξ are normalized by L and W, respectively, such that $0 \le \eta, \xi \le 1$. In the infinitely long case, the prescribed temperature boundaries are replaced by a temperature gradient.
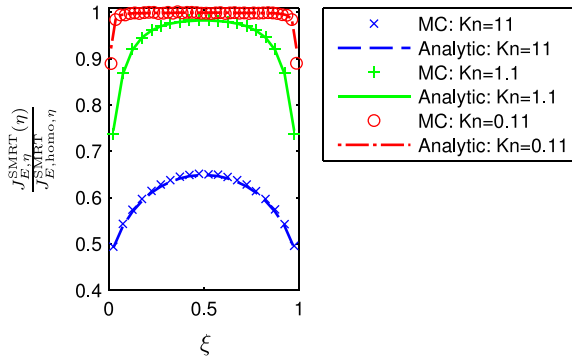
FIG. 7. Axial heat flux variation in the transverse direction in infinitely long graphene ribbons of various widths. Comparison between the analytical solution (lines) from Eq. (31) and the (SMRT) LAIP-LVDSMC results (symbols).

Size effects will be quantified by defining an effective thermal conductivity

$$\kappa_{\text{eff}} = -\frac{\bar{J}_{E,\eta} L}{\Delta T_\eta}, \qquad (35)$$

where $\bar{J}_{E,\eta}$ is the width-averaged heat flux in the ribbon axial direction and ΔT_η is the temperature difference applied along the ribbon ($T_h - T_c$ in Figure 5).

We expect kinetic effects to be dependent on the length-based and width-based Knudsen numbers, $Kn_L = \Lambda/L$ and $Kn_W = \Lambda/W$, respectively. Here, the mean free path was defined and calculated from

$$\Lambda = \sum_i^{N_{\text{states}}} \frac{v_i n_i^0}{B_{ii}} \Big/ \sum_i^{N_{\text{states}}} n_i^0. \qquad (36)$$

For fine discretizations, the mean free path depends weakly upon the reciprocal space discretization and essentially converges to $\Lambda \approx 0.6 \mu m$ at a discretization of $N_{\text{states}} = 38387$, in good agreement with other predictions of the graphene mean free path.[4] We also note that our computational results presented below indicate the presence of a diffusive to ballistic transition regime between the lengthscales of 5 μm and 50 nm, which is consistent with this mean free path estimate.

To scale out any dependence on reciprocal space discretization, in what follows, our results will be normalized by bulk properties calculated using the same discretization. For example, in Sec. VI A discussing infinitely long ribbons of finite width, the heat flux will be normalized by the expected value of this quantity for an infinitely wide ribbon, obtained using the same reciprocal space discretization and denoted $J_{W\to\infty,E}$. Similarly, in all sections except Sec. VI C, values of the effective thermal conductivity will be normalized by the bulk thermal conductivity, κ, (obtained using the same reciprocal space discretization). The effect of this normalization was investigated by numerical experiments, which show that at $Kn_W \approx 1$ the normalized effective thermal conductivity, $\kappa_{\text{eff}}/\kappa$, changes by less than 2.5% when the discretization is increased from $N_{\text{states}} = 5397$ to $N_{\text{states}} = 14997$. All results presented below are calculated using $N_{\text{states}} = 5397$.

A. Infinitely long ribbons

In this section, we consider ribbons that are sufficiently long ($Kn_L \to 0$) that they can be approximated as having infinite length. As explained in Sec. V C (where the SMRT scattering operator was applied to the same geometry), simulation of this geometry can be simplified by using a variable control temperature in the axial direction and solving only for variations in the transverse ribbon dimension.

Figure 8 shows (cell averaged) heat flux profiles obtained from our simulations of such systems, for various values of the Knudsen number $Kn_W = \Lambda/W$.

Figure 9 shows how the resulting effective conductivity of the ribbon, $\kappa_{\text{eff}} = \kappa \int_0^1 (J_E/J_{W\to\infty,E}) \mathrm{d}\xi$, varies as a function of Kn_W. This figure compares MC simulation results with those obtained using the iterative solution of the homogeneous Boltzmann equation,[46] in which the transverse boundaries are accounted for by augmenting phonon self-scattering with an additional scattering rate; for a rectangular ribbon this additional rate is given[77] by $2v_i|\sin(\theta_i)|/W$. The figure shows that the homogeneous approximation underpredicts the thermal conductivity by as much as 30% near $Kn_W = 1$.

B. Infinitely wide ribbons

In this section, we consider infinitely wide ribbons (L finite and $W \to \infty$) subject to an axial temperature gradient via prescribed temperatures of T_h and T_c at $\eta = 0$ and $\eta = 1$, respectively. Figure 10 shows our simulation results for the ribbon effective thermal conductivity for a wide range of Kn_L. The effective thermal conductivity approaches the homogeneous material value in the $Kn_L \ll 1$ limit and the ballistic (no intrinsic scattering) analytical result[75,76] in the $Kn_L \gg 1$ limit.

Our results also show that the approach to the ballistic limit is very slow (e.g., at $Kn_L = 10$, the difference between the theoretical ballistic limit and simulation results is on the order of 30%), presumably due to the very wide range of free paths associated with the *ab initio* scattering operator.

C. Ribbons of finite length and width

In this section, we consider graphene ribbons with finite length and width ($0.1 < Kn_W, Kn_L < 10$). In particular, we simulate axial heat transport due to an applied temperature
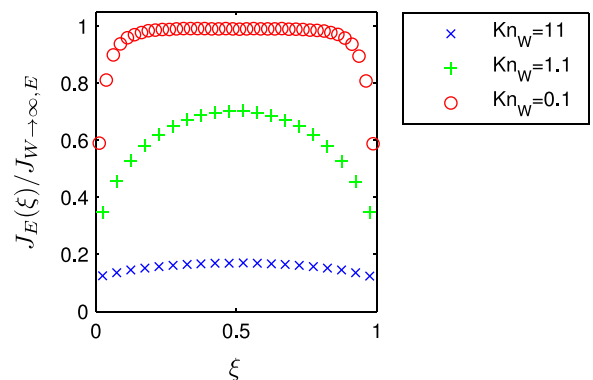

FIG. 8. LAIP-LVDSMC simulation results of the axial heat flux across graphene ribbons of various widths.
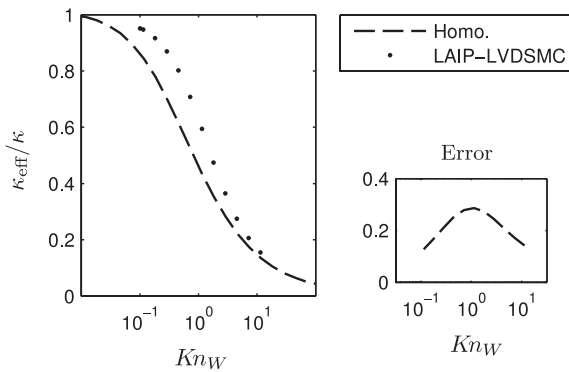
FIG. 9. Effective thermal conductivity for an infinitely long ribbon. Comparison between LAIP-LVDSMC simulation results and deterministic solution of the homogeneous BPE (augmented self-scattering).

FIG. 11. Comparison between LAIP-LVDSMC results (dashed line) and the experiments of Xu *et al.*[8] in finite-size graphene ribbons.

gradient using prescribed temperature boundaries as in the case of infinitely wide ribbons, but explicitly simulate transverse boundaries as diffusely reflecting walls. Because a bulk thermal conductivity value is not available from the experiments, in order to compare with the experimental results, in this section, we report unnormalized values of κ_{eff}. We note that the difference in bulk thermal conductivity with $N_{\text{states}} = 5397$ and the approximately converged value in Table II is 9%, which is well within the uncertainty of the experimental measurements.

We use our simulations to investigate the effect of finite ribbon width and, in particular, the approximation introduced by Xu *et al.*,[8] who performed experiments with ribbons of width 1.5 μm ($Kn_W \approx 0.4$) as approximations to infinitely wide ribbons. Comparison of LAIP-LVDSMC simulations of infinitely wide ribbons (data in Figure 10) and ribbons of width 1.5 μm (data in Figure 11) show that the error inherent in this approximation is acceptable for short ribbons, but not necessarily for long ribbons. Specifically, our simulations show that for $Kn_L > 1$ the error (that is, the difference in effective thermal conductivity between ribbons with $Kn_W = 0.4$ and ribbons with $Kn_W \to 0$) is on the order of 5%. On the other hand, this difference continues to grow as Kn_L decreases and becomes on the order of 20% at $Kn_L \approx 0.1$.

Figure 11 shows a comparison between the experimental results of Xu *et al.*[8] (at a temperature of 300 K and assuming 11.5% contact resistance) and our simulations of ribbons of

varying length and fixed width (1.5 μm). The two sets of results are in good agreement, particularly for short ribbons. This level of agreement is encouraging considering the very large scatter in both numerical and experimental data published over the last few years and verifies that significant kinetic (ballistic) effects are present in graphene ribbons with length scales from hundreds of nanometers to nearly tens of microns. Additional simulation results for ribbons of finite length and width can be found in Ref. 78.

VII. DISCUSSION

We have presented a method for solving the Boltzmann equation with *ab initio* scattering for temporally and spatially varying problems. Dispersion relations and transition rates were obtained from DFT calculations. The scattering algorithm developed is exactly energy conserving—a feature that is highly desirable in particle simulation methods, but incompatible with numerically derived scattering rates that do not strictly conserve energy. We presented an approximate method for reconciling these differences, and note that, provided scattering rates strictly conserve energy, LAIP-LVDSMC can use force constants calculated from DFT, empirical potentials, and possibly other methods. Clearly, the fidelity of the simulated results will depend on the quality of the material model. We hope that the present work will spur the development of highly accurate and self-consistent (energy conserving) scattering rates.

The method was used to simulate heat transport in graphene ribbons. We have considered very long ribbons of finite width, very wide ribbons of finite length and ribbons of finite length and width. For infinitely long ribbons, our results show that using a homogeneous scattering approximation underpredicts the effective thermal conductivity in the transition regime $0.1 \leq Kn_W \leq 10$ by an amount on the order of 10%, with a maximum of 30% at $Kn_W \approx 1$. Our simulations of two dimensional ribbons of finite length and width have been found to be in good agreement with the recent experimental data of Xu *et al.*[8] The level of agreement is particularly encouraging, considering the very large scatter in both numerical and experimental data published over the last few years. One of the major reasons for this large scatter is the number of approximations introduced as a means of
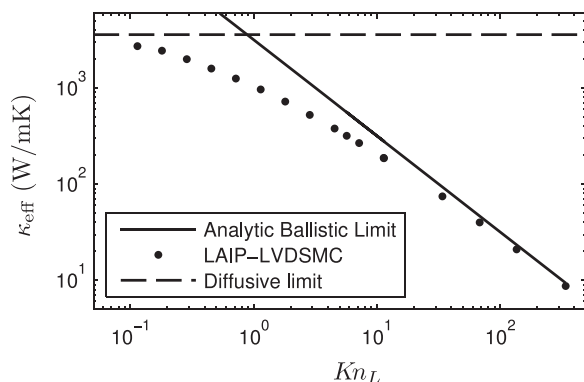

FIG. 10. Effective thermal conductivity of finite length ribbon calculated from the LAIP-LVDSMC method. Also shown is the analytic ballistic limit[76] as well as the homogenous material limit, both for the same discretization.
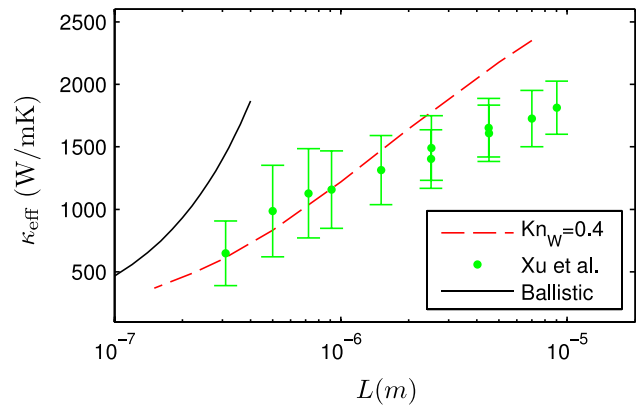
making these calculations or experiments possible. For example, in the case of Xu *et al.*, experiments were performed on ribbons of width 1.5 μm that were assumed to be sufficiently wide that width effects could be neglected; however, our results show that this approximation leads to an underestimation of the thermal conductivity by as much as 20% at $Kn_L \approx 0.1$. Efficient Boltzmann solutions methods using *ab initio* scattering will be invaluable in the future for providing means of analyzing transport in two-dimensional but also three-dimensional materials.

We note that the method for treating the *ab-initio* collision operator developed here is general and does not rely on assumptions about the material dimensionality; as a result, in principle it can be readily extended to three dimensions. Similarly, the particle formulation for integrating the advection part of the Boltzmann equation readily extends to three dimensions. The cost of the method will clearly be larger in three dimensions, primarily due to the increase of states in the reciprocal space discretization; we note, however, that despite their large computational cost, calculations involving three dimensional scattering operators are already being performed for deterministic solutions of spatially homogeneous problems.[42,46,47]

In closing, we note that Monte Carlo methods, as opposed to deterministic approaches, do not need to discretize reciprocal space. In this work, reciprocal space was discretized to allow for tabulation of the interaction term $\tilde{\mathcal{V}}_3(\lambda, \lambda', \lambda'')$, since real-time calculation of this term in continuous reciprocal space is prohibitively costly. Development of an efficient continuous representation of $\tilde{\mathcal{V}}_3(\lambda, \lambda', \lambda'')$ and a corresponding particle method for the scattering—as described by the linearized operator used in this work or its non-linear counterpart (Eq. (2))—could lead to significantly more efficient Monte Carlo algorithms and be particularly useful for three dimensional problems.

ACKNOWLEDGMENTS

[1]K. S. Novoselov, A. K. Geim, S. V. Morozov, D. Jiang, Y. Zhang, S. V. Dubonos, I. V. Grigorieva, and A. A. Firsov, Science **306**, 666 (2004).
[2]S. Chen, A. L. Moore, W. Cai, J. W. Suk, J. An, C. Mishra, C. Amos, C. W. Magnuson, J. Kang, L. Shi, and R. S. Ruoff, ACS Nano **5**, 321 (2011).
[3]J.-U. Lee, D. Yoon, H. Kim, S. W. Lee, and H. Cheong, Phys. Rev. B **83**, 081419 (2011).
[4]E. Pop, V. Varshney, and A. K. Roy, MRS Bull. **37**, 1273 (2012).
[5]L. A. Jauregui, Y. Yue, A. N. Sidorov, J. Hu, Q. Yu, G. Lopez, R. Jalilian, D. K. Benjamin, D. A. Delk, W. Wu, Z. Liu, X. Wang, Z. Jiang, X. Ruan, J. Bao, S. Pei, and Y. P. Chen, ECS Trans. **28**, 73 (2010).
[6]P. Wang, B. Gong, Q. Feng, and H.-T. Wang, Acta Mech. Sin. **28**, 1528 (2012).
[7]S. Chen, Q. Wu, C. Mishra, J. Kang, H. Zhang, K. Cho, W. Cai, A. A. Balandin, and R. S. Ruoff, Nat. Mater. **11**, 203 (2012).
[8]X. Xu, L. F. C. Pereira, Y. Wang, J. Wu, K. Zhang, X. Zhao, S. Bae, C. Tinh Bui, R. Xie, J. T. L. Thong, B. H. Hong, K. P. Loh, D. Donadio, B. Li, and B. Özyilmaz, Nat. Commun. **5**, 3689 (2014).
[9]L. Lindsay, D. A. Broido, and N. Mingo, Phys. Rev. B **82**, 115427 (2010).
[10]J. H. Seol, I. Jo, A. L. Moore, L. Lindsay, Z. H. Aitken, M. T. Pettes, X. Li, Z. Yao, R. Huang, D. Broido, N. Mingo, R. S. Ruoff, and L. Shi, Science **328**, 213 (2010).
[11]Z. Aksamija and I. Knezevic, Appl. Phys. Lett. **98**, 141919 (2011).
[12]D. Singh, J. Y. Murthy, and T. S. Fisher, J. Appl. Phys. **110**, 094312 (2011).
[13]D. Singh, J. Y. Murthy, and T. S. Fisher, J. Appl. Phys. **110**, 113510 (2011).
[14]L. Lindsay, W. Li, J. Carrete, N. Mingo, D. A. Broido, and T. L. Reinecke, Phys. Rev. B **89**, 155426 (2014).
[15]Y. Xu, Z. Li, and W. Duan, Small **10**, 2182 (2014).
[16]Y. Lu and J. Guo, Appl. Phys. Lett. **101**, 043112 (2012).
[17]S.-H. Tan, L.-M. Tang, Z.-X. Xie, C.-N. Pan, and K.-Q. Chen, Carbon **65**, 181 (2013).
[18]A. A. Balandin, S. Ghosh, W. Bao, I. Calizo, D. Teweldebrhan, F. Miao, and C. N. Lau, Nano Lett. **8**, 902 (2008).
[19]S. Ghosh, I. Calizo, D. Teweldebrhan, E. P. Pokatilov, D. L. Nika, A. A. Balandin, W. Bao, F. Miao, and C. N. Lau, Appl. Phys. Lett. **92**, 151911 (2008).
[20]S. Chen, Q. Li, Y. Qu, H. Ji, R. S. Ruoff, and W. Cai, Nanotechnol. **23**, 365701 (2012).
[21]S. Lepri, R. Livi, and A. Politi, Phys. Rep. **377**, 1 (2003).
[22]L. Yang, P. Grassberger, and B. Hu, Phys. Rev. E **74**, 062101 (2006).
[23]D. L. Nika, E. P. Pokatilov, A. S. Askerov, and A. A. Balandin, Phys. Rev. B **79**, 155413 (2009).
[24]A. A. Balandin, Nat. Mater. **10**, 569 (2011).
[25]S. Ghosh, W. Bao, D. L. Nika, S. Subrina, E. P. Pokatilov, C. N. Lau, and A. A. Balandin, Nat. Mater. **9**, 555 (2010).
[26]L. L. Baker and N. G. Hadjiconstantinou, Phys. Fluids **17**, 051703 (2005).
[27]T. M. M. Homolle and N. G. Hadjiconstantinou, J. Comput. Phys. **226**, 2341 (2007).
[28]G. A. Radtke, N. G. Hadjiconstantinou, and W. Wagner, Phys. Fluids **23**, 030606 (2011).
[29]J.-P. M. Péraud, "Low variance methods for Monte Carlo simulation of phonon transport," M.S. dissertation (Massachusetts Institute of Technology, Cambridge, MA, 2011).
[30]J.-P. M. Péraud, C. D. Landon, and N. G. Hadjiconstantinou, Annu. Rev. Heat Trans. **17**, 205 (2014).
[31]J.-P. M. Péraud, C. D. Landon, and N. G. Hadjiconstantinou, Mech. Eng. Rev. **1**, FE0013 (2014).
[32]R. Peierls, "On the kinetic theory of thermal conduction," in *Selected Scientific Papers of Sir Rudolf Peierls With Commentary*, edited by R. H. Dalitz and R. Peierls (World Scientific, Singapore, 1997), pp. 15–48.
[33]J. M. Ziman, *Electrons and Phonons* (Oxford Clarendon Press, 1960).
[34]G. P. Srivastava, *The Physics of Phonons* (CRC Press, 1990).
[35]K. Esfarjani, G. Chen, and H. T. Stokes, Phys. Rev. B **84**, 085204 (2011).
[36]G. Chen, *Nanoscale Energy Transport and Conversion* (Oxford University Press, 2005).
[37]D. G. Cahill, W. K. Ford, K. E. Goodson, G. D. Mahan, A. Majumdar, H. J. Maris, R. Merlin, and S. R. Phillpot, J. Appl. Phys. **93**, 793 (2003).
[38]E. Muñoz, J. Lu, and B. I. Yakobson, Nano Lett. **10**, 1652 (2010).
[39]A. S. Nissimagoudar and N. S. Sankeshwar, Phys. Rev. B **89**, 235422 (2014).
[40]M. G. Holland, Phys. Rev. **95**, 2461 (1963).
[41]M. Asen-Palmer, K. Bartkowski, E. Gmelin, and M. Cardona, Phys. Rev. B **56**, 9431 (1997).
[42]J. A. Pascual-Gutiérrez, J. Y. Murthy, and R. Viskanta, J. Appl. Phys. **106**, 063532 (2009).
[43]M. Omini and A. Sparavigna, Physica B **212**, 101 (1995).
[44]D. A. Broido, M. Malorny, G. Birner, N. Mingo, and D. A. Stewart, Appl. Phys. Lett. **91**, 231922 (2007).
[45]A. Ward, D. A. Broido, D. A. Stewart, and G. Deinzer, Phys. Rev. B **80**, 125203 (2009).
[46]N. Mingo, D. Stewart, D. Broido, L. Lindsay, and W. Li, in *Length-Scale Dependent Phonon Interactions, Topics in Applied Physics* Vol. 128, edited by S. L. Shindé and G. P. Srivastava (Springer, New York, 2014), pp. 137–173.
[47]G. Fugallo, M. Lazzeri, L. Paulatto, and F. Mauri, Phys. Rev. B **88**, 045430 (2013).
[48]J.-P. M. Péraud and N. G. Hadjiconstantinou, Phys. Rev. B **84**, 205331 (2011).
[49]J.-P. M. Péraud and N. G. Hadjiconstantinou, Appl. Phys. Lett. **101**, 153114 (2012).
[50]C. D. Landon and N. G. Hadjiconstantinou, in Proceedings of the International Mechanical Engineering Congress and Exposition, Paper No. IMECE2012-87957, 2012.

[51]W. Wagner, Monte Carlo Methods Appl. **14**, 191 (2008).

[52]A. J. Minnich, Phys. Rev. Lett. **109**, 205901 (2012).

[53]L. L. Baker and N. G. Hadjiconstantinou, Int. J. Numer. Methods Fluids **58**, 381 (2008).

[54]J. P. Perdew and A. Zunger, Phys. Rev. B **23**, 5048 (1981).

[55]J. Maultzsch, S. Reich, C. Thomsen, H. Requardt, and P. Ordejón, Phys. Rev. Lett. **92**, 075501 (2004).

[56]M. Mohr, J. Maultzsch, E. Dobardžić, S. Reich, I. Milošević, M. Damnjanović, A. Bosak, M. Krisch, and C. Thomsen, Phys. Rev. B **76**, 035439 (2007).

[57]N. Mounet and N. Marzari, Phys. Rev. B **71**, 205214 (2005).

[58]A. R. L. Wirtz, Solid State Commun. **131**, 141 (2004).

[59]N. G. Hadjiconstantinou, G. A. Radtke, and L. L. Baker, J. Heat Transfer **132**, 112401 (2010).

[60]C. D. Landon, "A deviational Monte Carlo formulation of ab initio phonon transport and its application to the study of kinetic effects in graphene ribbons," Ph.D. dissertation, Massachusetts Institute of Technology, Cambridge, MA, 2014.

[61]S. I. Kurganskii, O. I. Dubrovskii, and E. P. Domashevskaya, Phys. Status Solidi B **129**, 293 (1985).

[62]G. Gilat and L. J. Raubenheimer, Phys. Rev. **144**, 390 (1966).

[63]N. Bonini, J. Garg, and N. Marzari, Nano Lett. **12**, 2673 (2012).

[64]S. Kitipornchai, X. Q. He, and K. M. Liew, Phys. Rev. B **72**, 075443 (2005).

[65]Y. Huang, J. Wu, and K. C. Hwang, Phys. Rev. B **74**, 245413 (2006).

[66]K. Aoki, S. Takata, and F. Golse, Phys. Fluids **13**, 2645 (2001).

[67]G. A. Bird, Phys. Fluids **6**, 1518 (1963).

[68]G. A. Bird, *Molecular Gas Dynamics and the Direct Simulation of Gas Flows* (Clarendon Press, 1994).

[69]S. Rjasanow and W. Wagner, *Stochastic Numerics for the Boltzmann Equation* (Springer-Verlag, Berlin, 2005).

[70]G. A. Radtke, "Efficient simulation of molecular gas transport for micro- and nanoscale applications," Ph.D. dissertation, Massachusetts Institute of Technology, Cambridge, MA, 2011.

[71]J. Callaway, Phys. Rev. **113**, 1046 (1959).

[72]W. Cai, A. L. Moore, Y. Zhu, X. Li, S. Chen, L. Shi, and R. S. Ruoff, Nano Lett. **10**, 1645 (2010).

[73]C. Faugeras, B. Faugeras, M. Orlita, M. Potemski, R. R. Nair, and A. K. Geim, ACS Nano **4**, 1889 (2010).

[74]Z. Wang and N. Mingo, Appl. Phys. Lett. **99**, 101903 (2011).

[75]A. Y. Serov, Z.-Y. Ong, and E. Pop, Appl. Phys. Lett. **102**, 033104 (2013).

[76]M.-H. Bae, Z. Li, Z. Aksamija, P. N. Martin, F. Xiong, Z.-Y. Ong, I. Knezevic, and E. Pop, Nat. Commun. **4**, 1734 (2013).

[77]A. J. H. McGaughey, E. S. Landry, D. P. Sellan, and C. H. Amon, Appl. Phys. Lett. **99**, 131904 (2011).

[78]C. D. Landon and N. G. Hadjiconstantinou, in Proceedings of the International Mechanical Engineering Congress and Exposition, Paper No. IMECE2014-36473, 2014.